Full Length Article

Investigation of simultaneous production of H_2 and separable carbon from CH_4 in a fluidised bed of $NiO/Ca_2Fe_2O_5/CaO$ particles

Karine Alkhatib [a], Made Santihayu Sukma [a], Stuart A. Scott [a], Yaoyao Zheng [a,b,*]

[a] Engineering Department, University of Cambridge, UK
[b] Faculty of Engineering, University of Nottingham, UK

ARTICLE INFO

ABSTRACT

This work investigated the possibility of simultaneous production of hydrogen/syngas and separable solid carbon in a fluidised bed by using CH_4-CO_2 cycles and exploring the carbon growth over solid catalytic particles of NiO/$Ca_2Fe_2O_5$/CaO. This two-stage process included i) stage I: H_2-rich gas and carbon were simultaneously generated from the interaction between CH_4 and NiO/$Ca_2Fe_2O_5$/CaO particles; and ii) stage II: the reduced/carbon-deposited particles were regenerated in CO_2. Following our previous successful demonstration of the process for stable hydrogen production over cycles, this study focused on the formation of solid carbon and aimed at understanding its growth mechanism as well as demonstrating the potential of using fluidisation as a means of automatic carbon separation. By tracking the carbon growth history and the change in phases of the reacted NiO/$Ca_2Fe_2O_5$/CaO particles at temperatures from 700 to 900 °C, we discovered the formation of various forms of nano-structured carbon from CH_4 conversion (e.g. partial oxidation, pyrolysis). These include carbon nanotubes (CNTs), carbon graphite sheets, carbon onions (CNOs), and carbon fibres. Amorphous carbon was also observed, particularly in the initial stage of CH_4 conversion. Higher temperatures like 800 °C and 900 °C gave faster kinetics of CH_4 conversion and more formation of solid carbon. Fe_3C phase was observed on the reduced catalytic particles and could act as an intermediate phase or carbon sink for carbon growth. The results suggested that other mechanisms for carbon deposition, such as directly over Fe sites, may also exist. Fluidisation with a higher U/U_{mf} ratio separated more carbon-rich fines from the bulk catalytic particles in the fluidised bed. Fluidising with air at 700 °C effectively removed amorphous carbon on the reacted catalytic particles, whilst structured carbon remained. Full separation and purification to obtain pure carbon require furthers optimisation of e.g. fluidisation parameters and material design.

1. Introduction

Hydrogen (H_2) serves as a critical component in our industrial processes and energy landscape, accounting for a global consumption of 95 Mt in 2022 [1]. Its role is well-established in refining, synthesis of chemicals (e.g. a feedstock for producing ammonia, methanol, and other chemicals), and as a reducing agent in e.g. the steel industry. With a carbon-free nature, H_2 has recently sparked significant discourse regarding its expanded application in sectors such as transportation and production of hydrogen-based fuels (e.g. ammonia). This will lead to an annual growth in H_2 demand by 6 %, with expectations of exceeding 150 Mt by 2030 [1]. While investment in water electrolysis [1] for cleaner hydrogen production is on the rise, it is not yet feasible to fully supplant the use of traditional fossil fuels such as methane to satisfy the huge and

increasing demand. At least in the transition phase, it is imperative to explore sustainable utilisation of fossil fuels that aligns with carbon capture and storage, or, without generating gaseous carbon emissions. Methane (CH_4) still dominates the mass production of hydrogen with steam reforming (SMR) and CO_2 dry reforming (DMR) processes. Both SMR and DRM are energy-intensive due to their endothermic nature, necessitating high operating temperatures, typically between 750 to 1450 °C [2]. Partial oxidation of CH_4 (POM), which requires air separation to introduce oxygen for CH_4 conversion, is an alternative for producing hydrogen at lower temperatures with reduced energy costs due to its exothermic nature and faster kinetics [2]. Chemical looping (CL), using a solid oxygen carrier such as Fe_2O_3, presents another innovative approach to hydrogen production. CH_4 reacts with an oxygen carrier to reduce the solid material and produce syngas, or CO_2 ready for

sequestration in the first stage. H_2 is then produced through in a pure form by oxidising the reduced solids in the second stage, closing the loop. This separation of SMR into two steps enables separate control of reactions to favor thermodynamics and kinetics. Oxides like Fe, Ni, Cu, Mn have been actively studied for their compatibility in CL hydrogen production [3–8]. These technologies provide possibilities for installing post CO_2 capture facilities for reducing carbon emission purpose. However, this will be at a CO_2 capture cost of ~ \$15/tonne and up to ~ \$120/tonne [9].

Different from the above approaches that the carbon in CH_4 converts to gaseous byproduct as CO_2, the carbon source can also be turned into solid byproduct thereby avoiding the need for post CO_2 capture. Simultaneous production of H_2 and solid carbon products adds extra economic value to the utilisation of CH_4. The solid carbon materials, ranging from amorphous carbon to structured forms like graphite and carbon nanotubes (CNTs), have diverse industrial applications, with their value varying based on their structure and purity [10]. Amorphous carbon, like carbon black, is used as a reinforcing filler in rubber due to its good mechanical properties. Diamond, graphite, and their precursors such as CNTs are important structured carbons. Their prices vary from \$ 0.17/kg C for amorphous form, to > \$ 25 /kg C for graphite [10], and > \$ 200/kg C for CNTs [11]. The simplest method for simultaneous production of hydrogen and solid carbon is methane thermal pyrolysis, which involves breaking C–H bonds at high temperatures [12]. Researchers such as Abanades *et al.* [13] reported high CH_4 decomposition rates at 1350–1700 °C. Catalytic pyrolysis offers a lower-temperature alternative by using metal catalyst (*e.g.* Ni, Co, Fe) at temperatures no higher than 900 °C [12]. However, catalytic pyrolysis is often hindered by catalyst deactivation. Carbon-based catalysts (*e.g.* carbon black, activated carbon) have also been studied for methane pyrolysis, and such materials are more resistant to deactivation but with limited catalytic reactivity [12].

In addition to catalyst deactivation, another challenge of employing solid catalyst aiming for producing hydrogen and solid carbon products is the high cost associated with separating the deposited carbon from catalysts. Typical methods for separating carbon products include acid treatment, centrifugation, and selective solubilisation [14]. These post-processing methods impose a high cost for manufacturing applications, and more suited for purification purpose. Recently, there has been active investigations on using molten metal [10 15 16] and molten salts [17], to produce solid carbon separable from catalytic media. These molten processes allowed generating separable solid carbon (*e.g.* carbon black) from the catalytic media by forming a distinct carbon layer on top of the molten media, which can flow from the process columns and collected. In contrast to other processes with solid catalysts, using molten media necessitates higher operating temperatures above 1000 °C, meaning higher energy consumption.

Lowering the process temperatures and simplifying the process/reactor operating requirements will make the CH_4 to H_2 and separable carbon research more attractive towards industrial application. This prompts us to investigate the possibility of using a conventional chemical reactor with low-cost solid catalysts (such as Ni and Fe) for simultaneous production of hydrogen and separable carbon from methane. In this study, we combined Ni and Fe catalysts with CaO support to form a NiO/$Ca_2Fe_2O_5$/CaO material. The presence of CaO allowed $Ca_2Fe_2O_5$ to form; $Ca_2Fe_2O_5$ converting to Fe + CaO has a low equilibrium P_{O_2}, making it suitable for hydrogen production. Our previous work on hydrogen production from a fluidised bed of particles of NiO/$Ca_2Fe_2O_5$/CaO over CH_4-CO_2 cycling [18] observed whisker-like solid carbon on the catalytic particles, along with the stable production of hydrogen over 30 cycles. The production of H_2/syngas and solid carbon came from a combination of CH_4 pyrolysis and POM during the CH_4 processing stage. Interestingly, it seemed that not all the deposited carbon will deactivate the catalyst. The results suggested a synergistic effect of using this material, which contained CH_4 activation catalysts (*i.e.*, Ni and Fe), and a low P_{O_2} oxygen carrier ($Ca_2Fe_2O_5$) that protected locally reduced Ni or

Fe sites from deactivation by supplying lattice oxygen while not fully combusting CH_4. Further work is needed to address: 1) what types of carbon grows on Ni- and Fe-based catalytic particles in a fluidised bed? 2) how the carbons grow? 3) and whether the growth can be modified to allow carbon automatically, or easily, to fall off from the catalytic particles and thus to achieve simultaneous separation in a fluidised bed? Carbon growth on catalytic materials has been well studied in literature, with several widely recognised growth types, such as tip-growth and base-growth for CNTs [19,20] for methods like chemical vapour deposition. It is important to understand whether carbon grows in similar ways in a fluidised bed with catalysts coupled with oxygen carriers. This research, as an extension of our previous work on hydrogen production [18], examines the possibility of simultaneous producing hydrogen and separable solid carbon in a fluidised bed system at moderate temperatures (700 °C, 800 °C and 900 °C). This is achieved by qualifying and quantifying the carbon over NiO/$Ca_2Fe_2O_5$/CaO particles within the fluidised bed and the collected carbon fines out of the fluidised bed. The carbon growth mechanism on NiO/$Ca_2Fe_2O_5$/CaO is also examined.

2. Experimental

2.1. Material preparation

The preparation of NiO/$Ca_2Fe_2O_5$/CaO particles was described by Zheng *et al.* [18]. Briefly, powders of CaO (Fisher Scientific, >98 %) and Fe_2O_3 (Fisher Scientific, >98 %) were mixed at a Fe/(Ca + Fe) molar ratio of 0.4. Droplets of de-ionised (DI) water were added to the mixture to improve binding. A series of process including ball milling at 30 Hz for 3 h, drying at 120 °C, and calcination at 900 °C for 10 h, was conducted and repeated for 2 times to ensure good mixing and the formation of $Ca_2Fe_2O_5$/CaO particles. The resulting particles were sieved to 600–850 μm, before being mixed with nickel nitrate hexahydrate (Sigma-Aldrich, $Ni(NO_3)_2 \cdot 6H_2O$, ≥ 98.5 %) at a Ni/(Ni + Fe + Ca) molar ratio of 0.1. The NiO/$Ca_2Fe_2O_5$/CaO particles were then obtained upon further calcination at 550 °C for 5 h.

2.2. Fluidised bed reactor (FBR)

A FBR was built on a ceramic tube (i.d. 15 mm) placed within a furnace. 5 mL, or around 20 g of white fused alumina sand particles (Boud Minerals 355–425 μm), were loaded to the reactor at ambient temperature. Fig. 1 shows a schematic diagram of the FBR. Process gas entered the FBR from the bottom of the ceramic tube through a sinter. When the FBR reached a set temperature (700, 800, or 900 °C), around 2 g NiO/$Ca_2Fe_2O_5$/CaO particles (600–850 μm) were fed from its top. Alumina was used as an inert thermal reservoir [18] and mixed with the reacting particles of NiO/$Ca_2Fe_2O_5$/CaO. The gas inflow was controlled at 2 L/min (all gas flow rates expressed at 20 °C, 1 atm), which was selected to balance the total weight of the solids (NiO/$Ca_2Fe_2O_5$/CaO and alumina particles). The gas flow gave a ratio of fluidisation velocity/minimum velocity, U/U_{mf}, of 4.5 (at 700 °C) to 7.0 (at 900 °C), following Gibson *et al.* [21]'s modified correlation for predicting the onset of fluidisation. The solids inside the reactor were well fluidised and mixed by visual observation. The gas outflow was sampled at 1 L/min and went through a collection tube consisting of glass wool filter layers and $CaCl_2$ particles, before reaching the gas analysers (ABB) to measure CH_4, CO, CO_2 and H_2. This means any small solid particles and moisture in the sampled gas will be captured in the collection tube.

A typical experiment in the FBR consisted of two stages. In stage I, a flow of 20 % CH_4/N_2 reduced the catalytic material and produced H_2; in stage II, 30 % CO_2/N_2 regenerated the bed material. N_2 purged the reactor between the stages. At each temperature (unless otherwise stated), fresh NiO/$Ca_2Fe_2O_5$/CaO particles were first activated with 16 to 20 $CH_4 - CO_2$ cycles to obtain full reactivity. Typically, for one CH_4-CO_2 cycle, reduction in 20 % CH_4 was run for 15 min, and regeneration in 30 % CO_2 lasted for 30 min. After the material became fully activated,
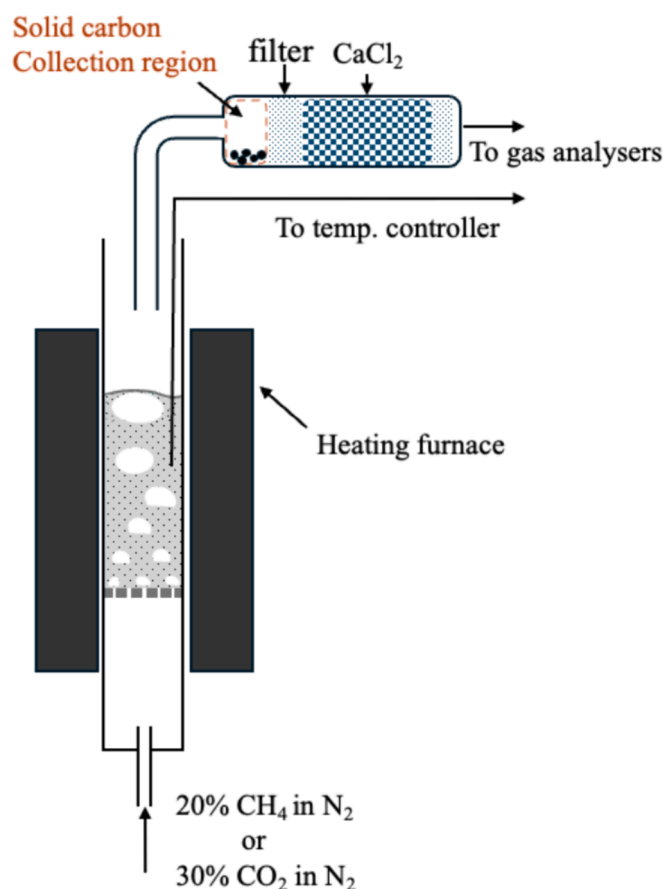
Fig. 1. Schematic diagram of the fluidised bed set-up.

a further 20 % CH$_4$/N$_2$ reduction stage was interrupted at different times, to examine the properties of the NiO/Ca$_2$Fe$_2$O$_5$/CaO particles and to track the build-up of carbon.

2.3. Material characterisation

The characteristics of carbon and carbon growing on the particle surface were analysed by Transmission Electron Microscopy (TEM) using the Thermo Scientific (FEI) Talos F200X G2 at 200 kV. Samples collected from the FBR, and the collection tube were positioned on a holey carbon coated 300 mesh Cu grid. TEM images were acquired using the Ceta 16 M CMOS camera and collected using the HAADF and BF detectors. The Super-X EDS detector system, consisting of 4 silicon drift detectors integrated in the X-TWIN objective lens, was used to generate EDS spectra and maps. The presence of disordered and graphitic forms of carbon was detected using the Horiba Scientific XploRA PLUS system with excitation at 532 nm. X-ray powder diffraction (XRD) analysis of samples was performed to identify the phases present at different time intervals during the 20 % CH$_4$ stage. The instrument was a Siemens Brucker D500; the parameters used were 20 mA, 35 kV, with a scan range from 10 to 90°, and a step size of 0.02°. Diffractograms were compared with references (Table S1) from the Inorganic Crystal Structure Database (ICSD) [22]. Refinement was conducted in MAUD.

3. Results

3.1. Material activation and carbon formation

Continuous CH$_4$-CO$_2$ cycling allowed the activation of fresh NiO/Ca$_2$Fe$_2$O$_5$/CaO particles. Fig. 2 presents the evolution of gas profiles during CH$_4$ reduction stage at 900 °C. After a few cycles, the gas profiles
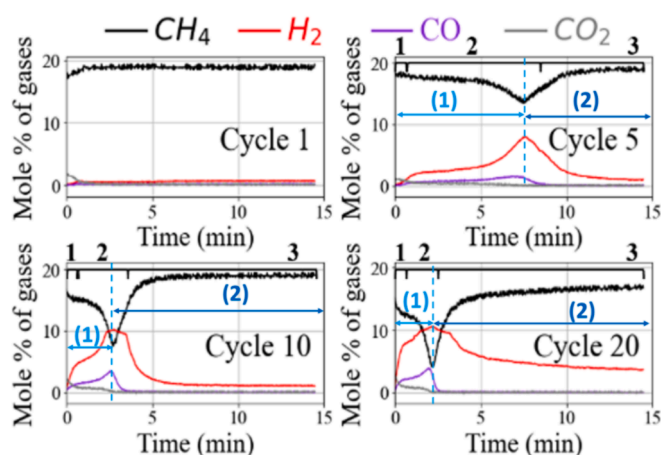
Fig. 2. Reduction of CH$_4$-CO$_2$ activation at 900 °C.

followed a trend that can split into two phases: in phase (1), a small amount of CO$_2$, and larger amounts of H$_2$ and CO were produced, with [H$_2$] and [CO] showing increasing trends; in phase (2), [CO] rapidly dropped and [H$_2$] showed a decreasing trend. Based on our previous study with activating NiO/Ca$_2$Fe$_2$O$_5$/CaO in a fluidised bed [18], phase (1) was governed by the partial oxidation and CH$_4$ cracking (R1, R2), with a small amount of full combustion to CO$_2$ from the interaction between CH$_4$ and NiO (R3). Phase (2) was governed by pure CH$_4$ cracking, with [CO] dropping to zero and the production of hydrogen continuing, but at a lower rate than its peak. From cycle 1 to cycle 20, the duration of phase (1), *i.e.* the time to reach phase (2) decreased, and the amount of H$_2$ increased, suggesting an increase in the reactivity of NiO/Ca$_2$Fe$_2$O$_5$/CaO particles. During CO$_2$ regeneration, as shown in Fig. 3, the increase in the produced [CO] (via R4-R6) from cycle 1 to 20 confirmed an increasing reactivity of the particles. This also indicates that the material either reduced to a deeper extent or allowed more carbon to deposit over cycles. Similar trend of increasing catalytic reactivity of NiO/Ca$_2$Fe$_2$O$_5$/CaO particles was reported for cyclic experiments with Ca$_2$Fe$_2$O$_5$ [23], without the presence of NiO.

$$Ca_2Fe_2O_{5(s)} + 3CH_{4(g)} \leftrightarrow 2CaO_{(s)} + 2Fe_{(s)} + 6H_{2(g)} + 3CO_{(g)} \tag{R1}$$

$$CH_{4(g)} \leftrightarrow C_{(s)} + 2H_{2(g)} \tag{R2}$$

$$4NiO + CH_{4(g)} \leftrightarrow 4Ni_{(s)} + 2H_2O_{(g)} + CO_{2(g)} \tag{R3}$$

$$2CaO + 2Fe + 3CO_2 \leftrightarrow Ca_2Fe_2O_5 + 3CO \tag{R4}$$

$$Ni + CO_2 \leftrightarrow NiO + CO \tag{R5}$$
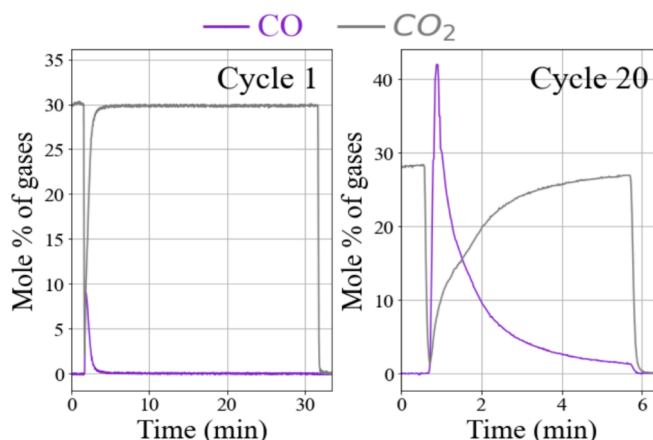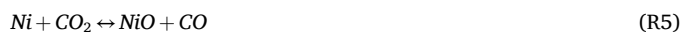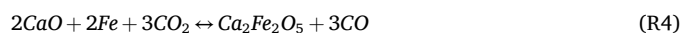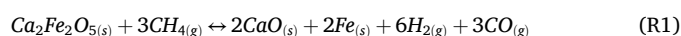
Fig. 3. Regeneration of CH$_4$-CO$_2$ activation at 900 °C.

$$C + CO_2 \leftrightarrow 2CO \tag{R6}$$

The deposited carbon over the $NiO/Ca_2Fe_2O_5/CaO$ particles was quantified via elemental balance on carbon (refer to S2). Fig. 4 shows the rate formation of carbon deposits (with their total deposition shown in Fig. S2). Comparing Figs. 2 and 4, the peak location of the rate of deposition appeared at similar positions where the conversion of CH_4 and the production of H_2 reached their maxima. This means that in phase (1), along with the partial oxidation of CH_4 to H_2 and CO, CH_4 cracking was significant and showed an increasing trend, leading to an increasing rate of carbon deposition. Thereafter, the carbon deposition rate dropped in phase (2), during which CH_4 cracking dominated and its partial oxidation was negligible. This suggests that the transfer of carbon in CH_4 to the solid phase does not necessarily need the full reduction of $NiO/Ca_2Fe_2O_5/CaO$. As soon as free reduced metal such as Ni and Fe (mostly via R1 and R3) became accessible, carbon started to deposit. Interestingly, the depletion of oxygen not only deactivated the partial oxidation but also quenched the reactivity of the material for converting CH_4 (refer to section 4 for discussion).

The fully activated $NiO/Ca_2Fe_2O_5/CaO$ particles, which experienced 20 CH_4-CO_2 cycles, then went through another reduction stage (i.e. 21st reduction). These particles, which experienced another 15 min reduction in FBR at 900 °C, were collected to observe carbon growth via TEM. Fig. 5 shows the formation of multi-walled CNTs (MWCNTs, images 1, 2, and 3), graphene sheets (image 4), and CNOs (images 5 and 6). MWCNTs exhibiting up to 25 walls, with a total thickness of 9.15 nm, were identified using a Ceta 16 M CMOS camera. These walls demonstrated a consistent and uniform thickness distribution, suggesting a thickness of 0.37 nm for one single layer. This is consistent with the literature findings for MWCNTs with a spacing varying between 0.27 to 0.42 nm [24], and close to a reported spacing of 0.34 nm when formed using a Fe-based catalyst [25]. The diameters of these CNTs, assessed at their base, are between 36.6 to 83.3 nm, comparable to those reported from other processes for generating CNTs from CH_4 cracking [26,27]. Furthermore, in our study, bamboo-shaped CNTs, which have a segmented structure whereby the tube appears divided into distinct cylinders, were observed (e.g. Fig. 5 Image 2). According to Sengupta and Jacob [27], using a Fe catalyst led to the formation of straight nanotubes, while Ni led to the formation of bamboo-shaped structures. Wang et al. [28] reported their results with Ni-Fe-SiO_2 catalyst and also obtained bamboo-shaped CNTs.

The retrieved particles from within the FBR have different forms of carbon and levels of carbon growth. Image 5 in Fig. 5 shows the initial formation of CNTs, while Image 2 presents significant growth of CNTs. CNTs formed by tip growth (Images 1 & 2), where the catalyst nanoparticles were pushed outwards from the main catalyst particle by the growth of carbon tubes, and base growth (Image 6), where tubes of carbon grew outwards and the catalyst nanoparticles remained at their base, were both observed. This indicates the presence of both weak and strong interactions between the nanoparticles and the main catalyst particles [29]. Image 6 displays both the presence of carbon whiskers/

fibers and carbon nano onions (CNOs), which are multiple concentric shells of fullerenes. Small Fe chunks were surrounded by concentric graphitic layers out of which fibers of carbon emerged. Sheet-like carbon was also observed (Image 4), which is one of the common carbon products from CH_4 cracking [30].

Zheng et al. [18] indicated that different carbon might deposit at different times during the reduction of $NiO/Ca_2Fe_2O_5/CaO$ particles by CH_4, not only when the particles were fully reduced to their metallic phases (e.g. Ni, Fe). To understand this further, here, particles at different reduction intervals, i.e. t = 5, 10 and 15 min, were collected to track carbon growth via Raman and XRD analysis. According to Fig. 6 (a), at t = 5 min, amorphous carbon was observed, as indicated by a prominent D peak (primary peak representing the disorder or defect [31]) and its modulation peaks at 1146.4 and 1426.5 cm^{-1} [32]. The presence of C – C bond (1000.78 cm^{-1}) suggests that within the initial 5 min, cracking of CH_4 took place and carbon atoms rearranged to form more complex compounds. At t = 10 min, the D peak was not found, while the modulation peaks (respectively identified at 1426.5 and 1429.5 cm^{-1} for two samples) of amorphous carbon showed high intensities, suggest change in carbon structure and disorder remained [33]. The peaks at t = 15 min (Fig. 6(c)) correspond to the formation of CNTs, marked with the appearance of a strong 2D peak at around 2700 cm^{-1} [32]. The ratio of peak intensities I_{2D}/I_G ratio is below 1, i.e. 0.90, reaffirming the presence of CNTs rather than graphene, which is typically characterised by $I_{2D}/I_G > 3$ [34]. The above results suggest amorphous and heavier carbon started to deposit from the beginning of the reduction, as the reaction proceeded, the particles developed the ability to produce structured carbons like CNTs at a deeper level of reduction.

Phase transitions in $NiO/Ca_2Fe_2O_5/CaO$ particles during the CH_4 reduction stage are shown in the XRD spectra (Fig. 7). At t = 0 min, when reduction had not started, only peaks of fully oxidised $Ca_2Fe_2O_5$, NiO, and CaO phases were observed. At t = 2 min, as reduction just started, peaks of Ni were shown, in addition to the presence of $Ca_2Fe_2O_5$, NiO, and CaO phases. This suggests exposed to CH_4, NiO reduced first, prior to the reduction of $Ca_2Fe_2O_5$. This is consistent with our previous study with reducing $NiO/Ca_2Fe_2O_5/CaO$ [18]. At t = 5 min, the phases observed remained the same (compared to t = 2 min), with only the intensities for each phase changed slightly. At t = 15 min, clear peaks of Fe_3C and Ni (or possible Ni-Fe alloys) were observed; stronger CaO peaks were shown. No peaks of $Ca_2Fe_2O_5$ were observed, suggesting full reduction of $Ca_2Fe_2O_5$ at t = 15 min. The presence of Fe was not identified in the XRD spectra, as the main peaks of Fe overlapped with peaks of Al mount. Fe might have formed; Sukma et al. [23] demonstrated that the reduction of $Ca_2Fe_2O_5$ was a single-phase transition directly to Fe and CaO. Here, it appears that a substantial amount of the iron produced by reduction goes on to form Fe_3C at 900 °C.

3.2. The effect of temperature

CH_4-CO_2 cycles were further conducted at 800 °C and 700°C. At 800 °C, a batch of fresh $NiO/Ca_2Fe_2O_5/CaO$ particles underwent 20 CH_4-CO_2 cycles and reached their maximum activity in the 10th cycle. The first few cycles (as shown in Fig. S3) followed a similar trend to those at 900 °C: in phase (1), H_2 and CO, is produced from the combination of partial oxidation and methane cracking; and in phase (2), mainly methane cracking to H_2 occurred. During the reduction stage in the 1st cycle at 800 °C, a small amount of CO_2 was observed in the beginning of reduction. This was also observed at 900 °C and is mainly due to the combustion of CH_4 by the NiO. The CO_2 peaks were not observed from the 2nd cycle and onwards at 800 °C, but were maintained at 900 °C. This could be explained by incapability of CO_2 to regenerate Ni to NiO at 800 °C. Fig. 8 presents the cyclic amount of total deposited carbon, estimated from the carbon balance (refer to S2). In general, the amount of solid carbon gradually increased over cycles and reached maximum at cycle 10.

The activated $NiO/Ca_2Fe_2O_5/CaO$ particles at 800 °C were then
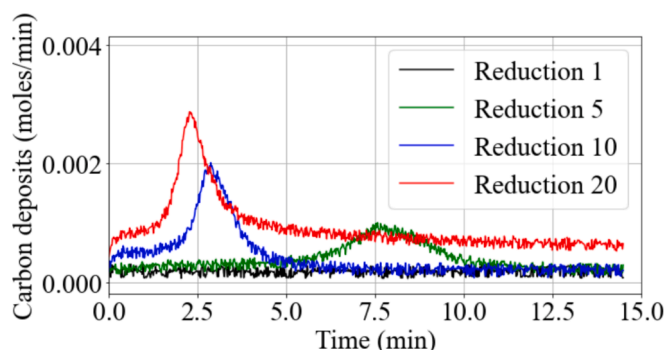
Fig. 4. Rate of deposition of carbon at 900 °C.
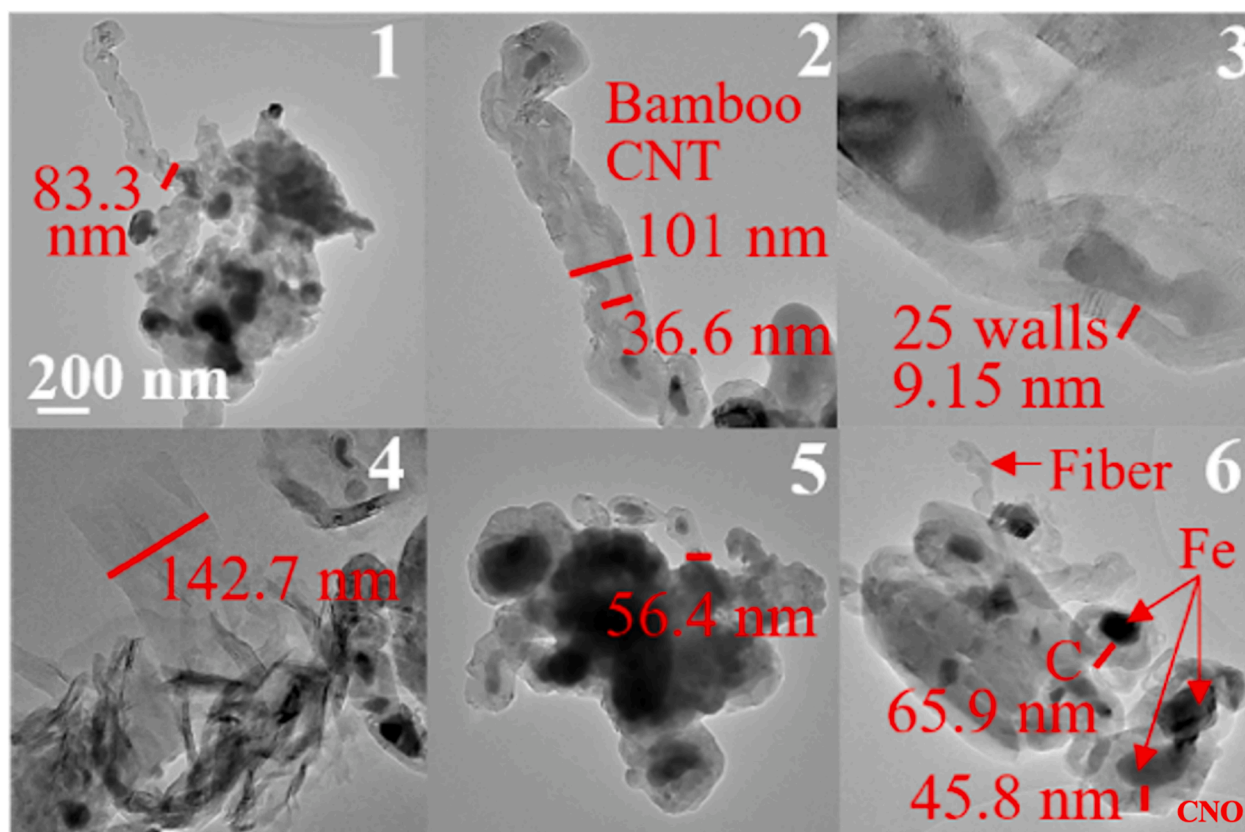
Fig. 5. TEM of particles collected from the FBR after 15 min of CH_4 reduction and 20 CH_4-CO_2 cycles, carried at 900 °C. The retrieved FBR particles were originally larger (600–850 um); during preparation for TEM analysis, the particles broke down easily to smaller ones, as shown here. The six images show different particles (Images 1, 4, 5, and 6), and different parts (Images 1, 2, and 3) of a same particle, processed from the same experimental conditions at 900 °C.
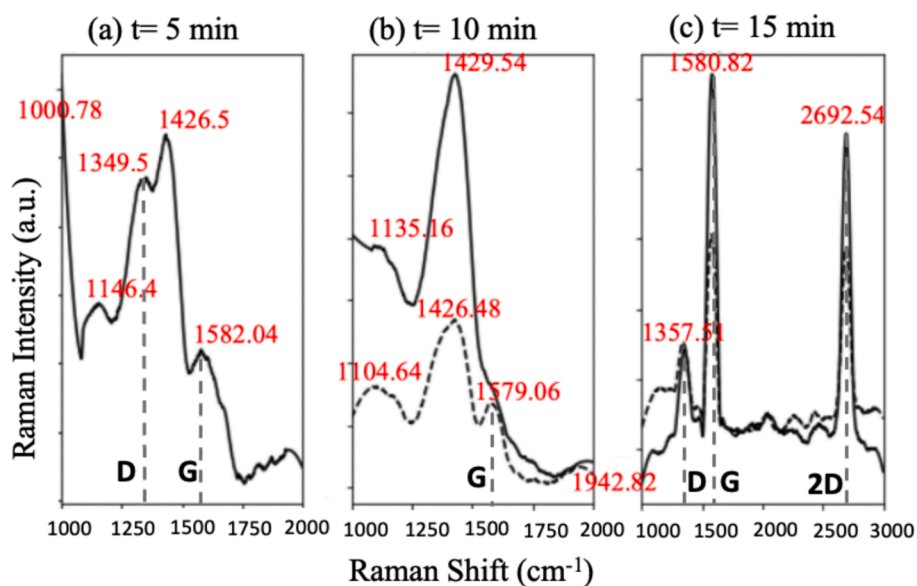
Fig. 6. Raman spectra of NiO/$Ca_2Fe_2O_5$/CaO in the 21st reduction at t = 5, 10, and 15 min at 900 °C respectively. Two lines were shown in both (b) and (c), and they represent results of two different particles for each case.

collected from the FBR to track the forms of carbon deposition (Fig. 9) and their phase transitions (Fig. 10). The Raman spectra in Fig. 9 demonstrates the presence of amorphous carbon (wide D band) at t = 0 min. This could be due to the remaining carbon from previous CH_4-CO_2 cycling at 800 °C. As time proceeded, peaks at around 1431.3 and 1445.1 cm^{-1} for t = 5 and 10 min respectively, were observed. These are

likely to be modulation peaks of amorphous carbon. The high intensity and widths of the modulation peaks make identifying any D peaks difficult. At t = 15 min, the primary D peak, which represents defects or amorphous phase, appears again. In addition, no G peak was observed in these cases, indicating the absence of graphitic carbon at 800 °C. The XRD spectra (Fig. 10) of the material reduced at different levels at 800 °C
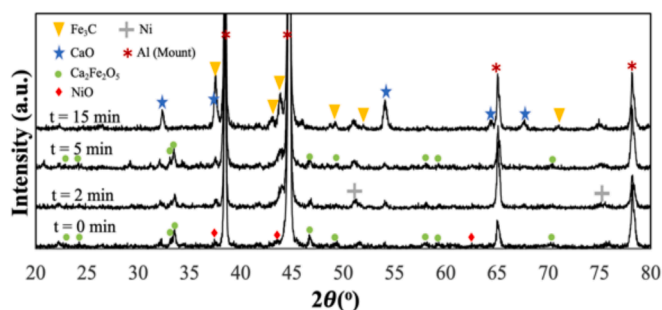
Fig. 7. XRD spectra of NiO/Ca₂Fe₂O₅/CaO in the 21st reduction at t = 0, 2, 5, and 15 min at 900 °C respectively.
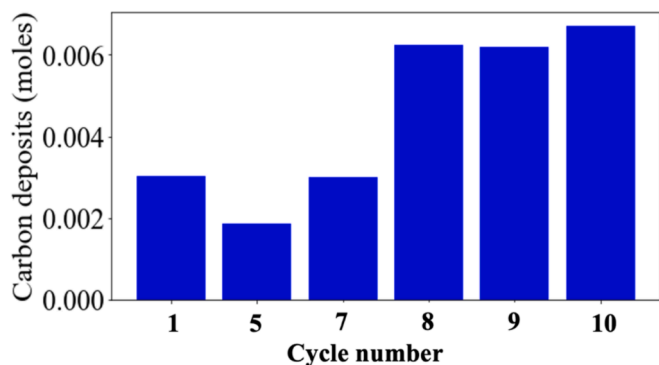
Fig. 8. Total deposition of carbon for each reduction at 800 °C.

show similar transition phases as those at 900 °C. As the reduction proceeded, stronger Ni peaks were observed. $Ca_2Fe_2O_5$ was gradually reduced, and its reduction has eventually led to the appearance of Fe_3C (from the interaction between CH_4/deposited carbon with Fe sites) and CaO, which was supported by an increase in the intensity of Fe_3C and CaO peaks.

At 700 °C, fresh $NiO/Ca_2Fe_2O_5/CaO$ particles were tested for 20 CH_4-CO_2 cycles, with no strong sign of material activation, and no CH_4 conversion. This suggests the activation requires higher temperature, *e. g.* 800 and 900 °C. Therefore, a batch of fresh $NiO/Ca_2Fe_2O_5/CaO$ particles were firstly fully activated at 900 °C (with 6 CH_4-CO_2 cycles), prior to its being used for simultaneous production of H_2 and solid carbon. At 700 °C, the gas profiles of the CH_4 reduction of fully activated $NiO/Ca_2Fe_2O_5/CaO$ particles were different (refer to Fig. S4) from those at

800 and 900 °C: there was a gradual increase in the activity of the material up to cycle 8, after which the activity started to fall. The total amount of deposited carbon from the CH_4 reduction stage of each cycle, generally decreased over cycles, as presented in Fig. 11. This reduced reactivity of $NiO/Ca_2Fe_2O_5/CaO$ for CH_4 cracking and conversion is likely due to the ineffective removal of deposited carbon by CO_2 at 700 °C, similar to, but more significant than that at 800 °C. This low capability of removing solid carbon at 700 °C was further supported by the low amount of CO released during the CO_2 regeneration stage, suggesting that the unremoved carbon would carry over to the next cycle.

Fig. 12 shows the Raman spectra of the catalyst examined at 0, 5, 10, and 15 min from exposing to CH_4 at 700 °C. At t = 0 min, strong G and 2D peaks with a I_{2D}/I_G of around 0.8, were seen. This indicates some CNTs remained after the regeneration in a previous (activation) cycle. A strong and sharp D peak was also observed, indicating high intensity of defects in carbon structure. The ratio of I_{2D}/I_G remained below 1 from t = 0 min to 15 min at 700 °C, suggesting likely presence of CNTs throughout the reduction. The XRD spectrum (Fig. 13) at t = 5 min showed phases of $Ca_2Fe_2O_5$, CaO, Ni and Fe_3C. These species remain in the particles reduced for 10 and 15 min. Slower kinetics mean that at 700 °C the reduction of $Ca_2Fe_2O_5$ at t = 15 min was incomplete.

3.3. Carbon separation

The above results presented simultaneous production of hydrogen and solid carbon in a fluidised bed, with different forms of carbon including amorphous and structured being found attached to the catalytic particles of $NiO/Ca_2Fe_2O_5/CaO$. One of the research aims was to
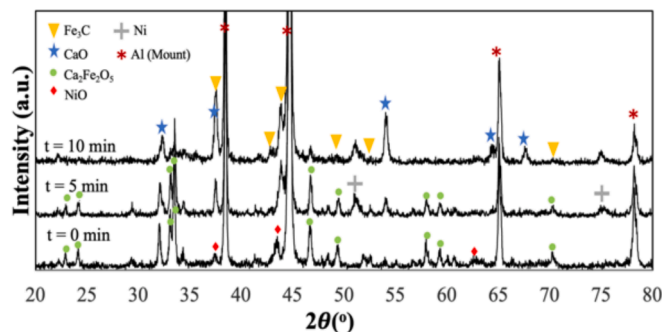
Fig. 10. XRD spectra of NiO/Ca₂Fe₂O₅/CaO in the 21st reduction at (a) t = 0, (b) t = 5, (c) t = 10 min at 800 °C.
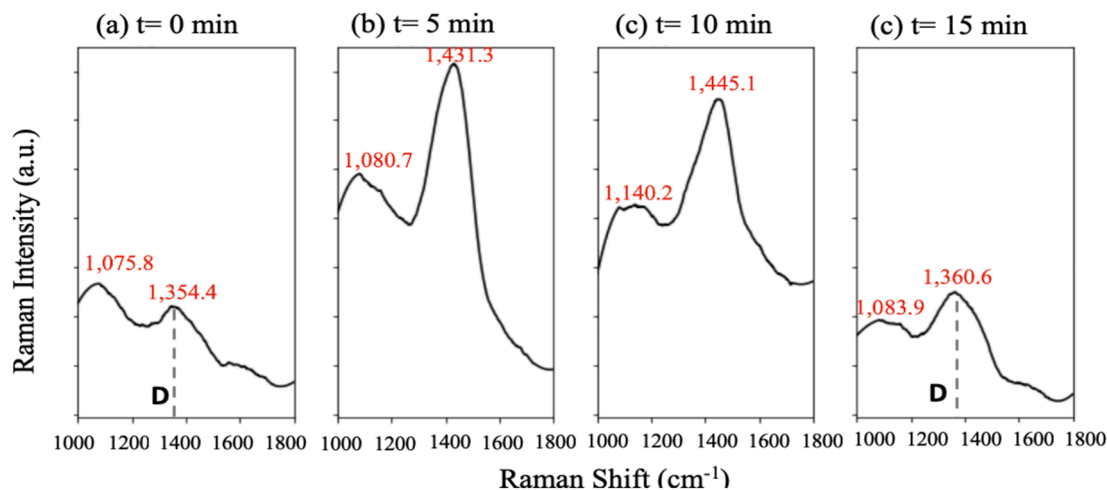
Fig. 9. Raman spectra of NiO/Ca₂Fe₂O₅/CaO in the 21st reduction collected at t = 0, 5, 10 and 15 min at 800 °C.
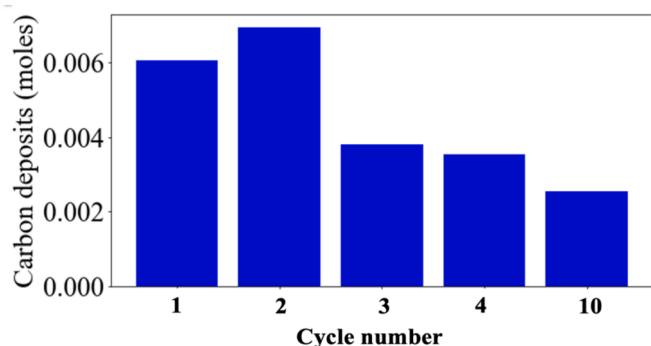
Fig. 11. Total deposition of carbon for each reduction at 700 °C.

investigate the possibility to achieve automatic separation of carbon from the catalytic particles. Therefore, a collection tube (as shown in Fig. 1) was positioned at the outlet of the FBR to collect any fines or small particles from the FBR. The fines from the collection tube were characterised to understand their distribution of carbon, and the results compared with the larger particles from the FBR (at different intervals of the reduction, retrieved after cooling the FBR). As shown in Fig. 14, at 900 °C, both the fines from the collection tube and the particles from within FBR showed the presence of carbon and the catalytic elements (Ni and Fe). The collection tube (B group) generally gave a much higher carbon content. Similar findings were found for 800 °C (refer to S5). At 700 °C, a low amount of solid fines were seen in the collection tube, suggesting insignificant separation of solid carbon from the NiO/Ca₂Fe₂O₅/CaO particles, or, a small amount of carbon formed. The particles retrieved from the FBR showed a large growth of carbon and significant surface coverage of carbon, as shown in Fig. S5C. This insignificant separation, or falling off, of the carbon fines from the main particles could be linked to the lower U/U_{mf} of 4.5 ± 0.3 at 700 °C (compared to 6.1 ± 0.2 at 800°C and 7.2 ± 0.4 at 900 °C), meaning less turbulence between the particles and gas bubbles within the FBR. Therefore, if suitable fluidisation conditions are met, such as at higher temperatures at 800 °C and 900 °C which gave higher U/U_{mf} and thus more external forces around/through the particles, it can promote simultaneous production of hydrogen and separable solid carbon.

The carbon fines from the collection tube at different process temperatures (700, 800, and 900 °C) contained both amorphous and structured carbon, as evidenced from their Raman analysis (Fig. S6). On the other hand, even though fluidisation helped to separate carbon-rich fines from the FBR, some carbon remained. The above findings led to the idea of using air to burn off some unstructured carbon (ideally amorphous carbon) and react this weakly connected carbon to allow the

structured carbon to fall off, hence achieving full separation of structured carbon products. This was investigated by introducing an air fluidising stage at 700 °C after the CH₄-CO₂ cycles at either 800 °C or 900 °C. Air post processing at a lower temperature, *i.e.* 700 °C, was intentionally selected to avoid combustion of all the structured carbons. The particles from the FBR (Fig. 15) and the solid fines from the collection tube (Fig. 16) were compared. Sheet-like carbon was observed in the particles from within the FBR. Comparing to the surface morphology of the catalytic particles without air stage, as shown in Fig. 5, less structured carbon was observed after air stage. The squares/rods (likely CaCO₃) seen in Fig. 15 might have resulted from cooling the CH₄-CO₂ cycled catalytic particles from 900 °C to 700 °C in CO₂ flow, before switching to air flow. TEM of solid fines from the collection tube, as presented in Fig. 16, shows mainly MWCNTs and CNOs with negligible amounts of amorphous carbon. Fig. 17 illustrates the distribution of all elements (Ca, O, Fe, Ni, and C). Around half of the Fe and Ni sites overlapped with most C sites. Structured carbon (*e.g.* CNTs in Fig. 17) attaching to these overlapped zones was seen. Linking these to the observation of Fe₃C from XRD results, suggests that Fe₃C plays a role in carbon growth. The propagation of the outgrowth of some structured carbon can be from Fe₃C. There are also some overlapped Fe and Ni sites free of carbon. This means in addition to Fe₃C, there were the presence of reduced Ni, Fe, or/and their alloys, which could also promote carbon growth (without forming carbide phases).

4. Discussion

Iron carbide (Fe₃C) was observed (Figs. 7, 10, and 13) during reduction at different temperatures. According to the Fe-C phase diagram [26], in the absence of carbon, below 912 °C, Fe is stable as body-
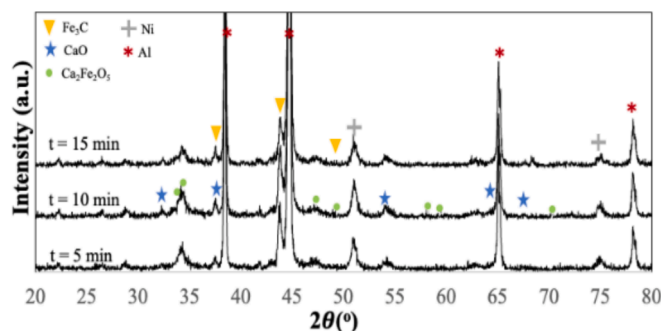
Fig. 13. XRD spectra of NiO/Ca₂Fe₂O₅/CaO in the 21st reduction at t = 5, 10, and 15 min at 700 °C.
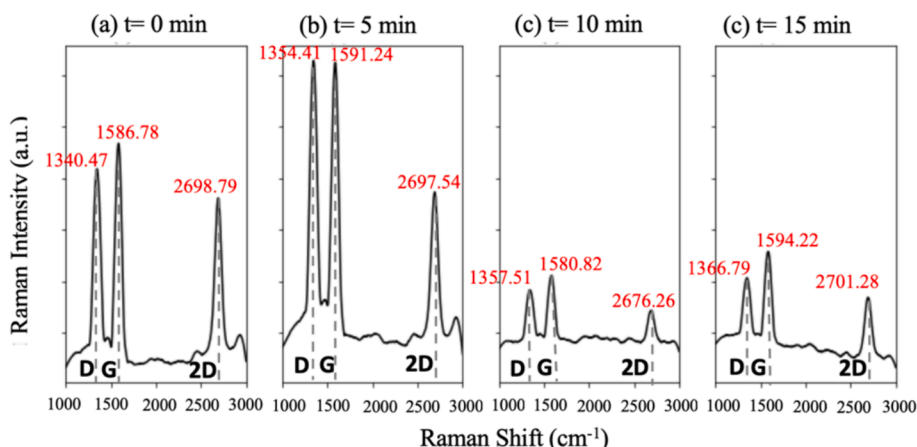
Fig. 12. Raman spectra of NiO/Ca₂Fe₂O₅/CaO in the 21st reduction at (a) t = 0, (b) 5, (c) 10, and (d) 15 min at 700 °C.
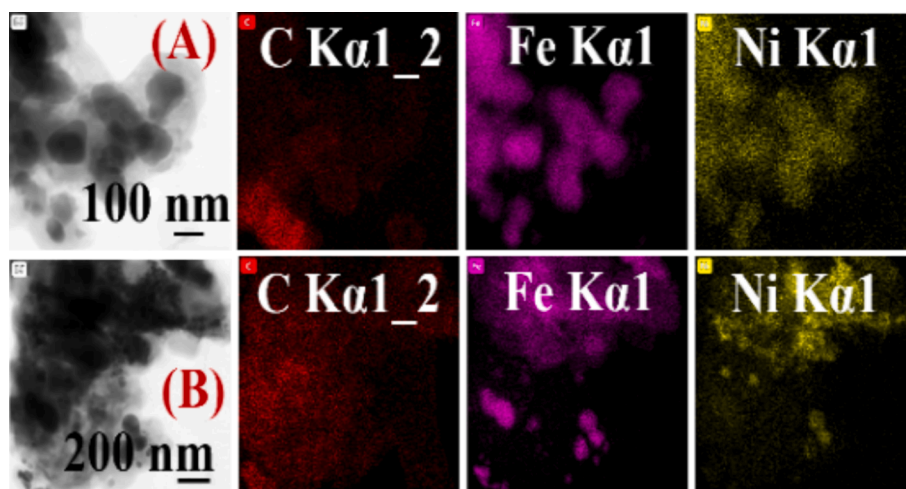
Fig. 14. TEM-EDS of samples collected from reactor (A) and collection tube (B) after 20 reduction-regeneration cycles followed by CH$_4$ reduction for 15 min at 900 °C.
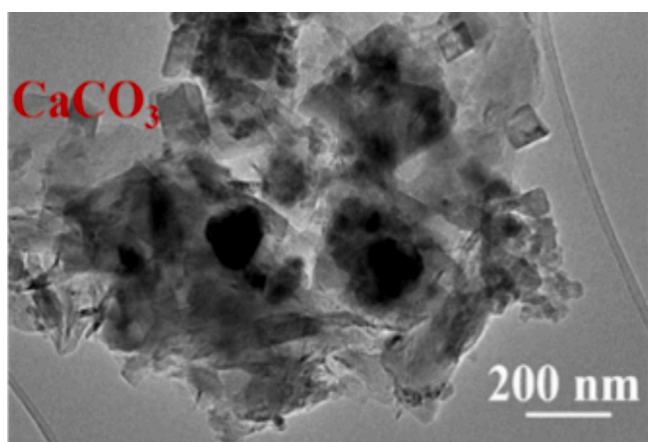
Fig. 15. TEM of particles collected from the reactor tube after air stage at 700 °C for 60 min, with the air flow rate of 2 L/min (expressed at 20 °C, 1 atm). Prior to air stage at 700 °C, the catalytic particles underwent CH$_4$-CO$_2$ cycles at 900 °C, and then cooled to 700 °C in CO$_2$ flow, before switching to air flow.

centered cubic α-Fe (ferrite), and above as face-centered cubic γ-Fe (austenite). When carbon is present, γ-Fe can form above 727 °C. At 700 °C, Fe$_3$C forms once the carbon content in the iron exceeds 0.02 wt% with the Fe$_3$C in equilibrium with α-Fe. The amount of carbon needed to form the Fe$_3$C is much greater at higher temperatures, *e.g.* 1.0 wt% for 800 °C and 1.4 wt% for 900 °C, and it precipitates from γ-Fe. Our results showed that higher temperatures like 800 and 900 °C gave faster kinetics and more carbon in the solid phase (either in Fe$_3$C or solid carbon). For instance, in the reduction of cycle 10, deposits amount to 0.007 mol at 900 °C (Fig. S2), 0.006 mol at 800 °C (Fig. 8), and 0.002 mol at 700 °C (Fig. 11). Based on the full reduction of Ca$_2$Fe$_2$O$_5$, the molar of Fe to C ratio would be 1.69, 1.97, and 5.92 for 900 °C, 800 °C and 700 °C respectively. These are equivalent to a carbon content of 11.2 wt% (900 °C), 9.8 wt% (800 °C), and 3.5 wt% (700 °C) in an iron-carbon binary system. The amounts of carbon at each temperature significantly exceed equilibrium amounts for forming Fe$_3$C, further supports the formation of Fe$_3$C and confirms significant growth of solid carbon (C). It should also be noted that in addition to Fe as a catalytic component for CH$_4$ conversion and carbon deposition, depositing carbon would also take place on active Ni sites. This means, the local ratio of C to Fe, may be lower.

There has been disagreement about whether the formation of intermediate Fe$_3$C is required for CNT growth [27]. The results here suggest that the formed Fe$_3$C could potentially serve as a carbon sink or catalytic site for further CH$_4$ cracking. A detailed mechanism by which α-Fe or γ-Fe transitioned into Fe$_3$C has been previously described [25,35]. When a CH$_4$ molecule reaches the catalyst surface, it breaks down into H$_2$ and amorphous carbon. Once the deposited carbon surpasses the solubility threshold, carburisation, the process through which amorphous carbon reacts with Fe to create Fe$_3$C, occurs. Fe$_3$C can act as new catalytic sites for CH$_4$ decomposition. As amorphous carbon continues to accumulate on Fe$_3$C, it would diffuse into the latter and is transferred into graphitic carbon [35]. Alternatively, Fukuhara *et al.* [25] proposed that Fe$_3$C could be unstable and decompose back into Fe and graphite. Amorphous carbon can migrate into the newly released Fe sites, nucleating to form filaments. Furthermore, Wirth *et al.* [26] earlier proposed that structured carbon formation could take place directly on Fe sites, without the formation of Fe$_3$C. This was based on the coupling a statistical
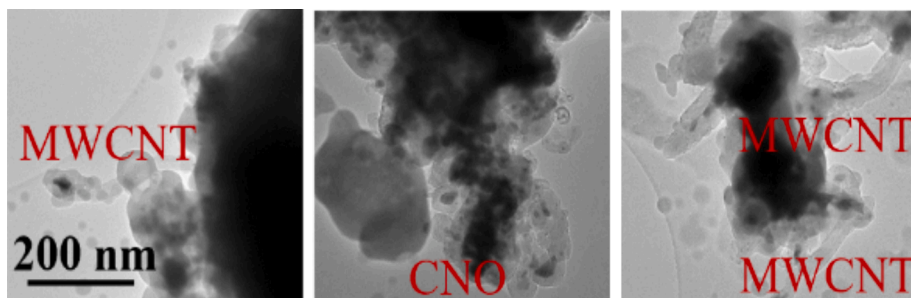
Fig. 16. TEM of solid fines retrieved from the collection tube after carbon/catalyst separation attempt with an air flow rate (2 L/min, expressed at 20 °C, 1 atm) at 700 °C for 60 min. The 3 images show different particles/solid fines collected from one experiment, with the same process conditions for Fig. 15.
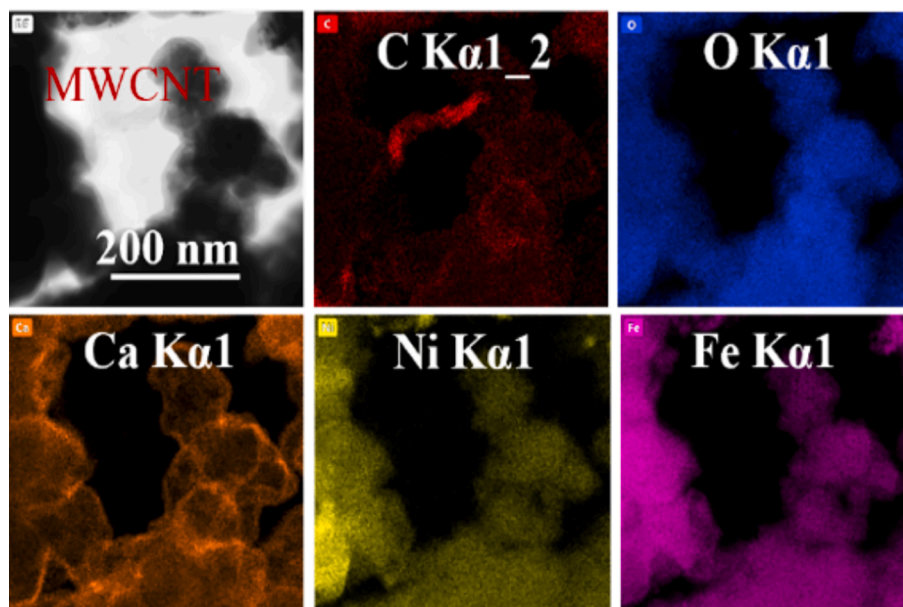
Fig. 17. EDS of solid fines retrieved from the collection tube after carbon/catalyst separation attempt with air at 700 °C.

estimation of carbon nucleation and the phase diagram of a Fe-Fe$_3$C-graphite system. For example, at 800 and 900 °C, at low carbon content, α-Fe and γ-Fe form in equilibrium. On increasing carbon content, γ-Fe is fully formed (and no α-Fe is present); further increase in the carbon content cause the formation of Fe$_3$C. Carbon nucleation will then occur, and the growth can proceed from γ-Fe. Growing carbon structures would then become a sink for excess carbon and ideally prevent γ-Fe from forming Fe$_3$C phase. In our study, both the presence of Fe$_3$C, carbon filaments/whiskers and graphitic carbon like CNTs (Fig. 5) were observed, suggesting the likelihood of multiple carbon formation mechanisms as a combined result of kinetic and thermodynamic effects.

The co-existence of several forms of structured carbon, as seen in Fig. 5, has been reported by *e.g.*, Jaworski *et al.* [36]. At lower temperatures (below 500 °C), the formation of encapsulating carbon (like CNOs), occurs through the gradual polymerisation of complex hydrocarbon radicals. In the temperature range of 447–597 °C, filamentous carbon structures become prevalent, and the formation of soot initiates at 597 °C. As temperatures rise to higher levels (800–1000 °C), carbon filaments develop on catalysts such as Ni or Fe, facilitated by the presence of hydrogen. Conversely, in reactions involving pure CO, the dominance of encapsulating carbon structures became more pronounced at these elevated temperatures. Fig. 5 shows that the growing structures have encapsulated particles. There have been several attempts to explain the encapsulation of materials in growing CNTs. A weak interaction between the active site and support promotes tip growth, wherein the catalyst particle is carried upwards by the developing CNT. Conversely, strong support materials favor base growth, wherein the CNT growth proceeds through an open tip [29]. The size of the catalyst particle also plays a role in determining the growth mechanism. Larger Ni and Fe particles tend to induce more tip growth of carbon, whereas smaller particles are more likely to become encapsulated by the growing carbon during CNT formation [29]. Therefore, a mix of large and small Fe and Ni sites/particles could also contribute to the formation of both tip and base-growth CNTs. Zhou *et al.* [35] discussed the effect of reaction rate within FBR. As the reaction rate increased, a compressive force at the bottom of the catalyst particles started to overcome the surface tension. In this scenario, the stretched portion of the catalyst loses its ability to retract and consequently might get drawn into the growing carbon nanotube. This could result in the formation of nanotubes with periodic jumps of catalyst particles at regular intervals. At extremely high reaction rates, the precipitation of

graphite could occur at an accelerated pace. The intensified compressive forces overwhelm the surface tension of the catalyst, leading to the complete encapsulation of the catalyst by the graphite. As a result, structures like CNOs would form.

In contrast to conventional simultaneous production of hydrogen and separable carbon from catalytic metals or molten salts, this study used materials containing conventional catalytic components (Ni and Fe) for activating CH$_4$ but also with their oxidised form with lattice oxygen. Though the presence of lattice oxygen may have diluted slightly the concentration of H$_2$ in the gas phase by generating CO, however, according to Figs. 2 and 4, it allowed to generate more hydrogen and solid carbon. This could be explained by the transient equilibrium state between the metallic catalytic forms (*e.g.* Ni or/and Fe) and the lattice oxygen in Ca$_2$Fe$_2$O$_5$. This transient phenomenon was firstly proposed by Zheng *et al.* [37] on H$_2$ production from CH$_4$ with NiO/Fe$_2$O$_3$ particles. The lattice oxygen helped to maintain a transient NiO/Ni equilibrium state and thus the production of H$_2$ was maintained at a high yield. In this study, both Ni and Fe sites might have been kept transiently active for converting CH$_4$ to produce hydrogen and solid carbon through the transfer of lattice oxygen in the Ca$_2$Fe$_2$O$_5$ to the Ni and Fe sites. It is likely that the growth of carbon with catalysts support on an oxygen carrier might differ from the carbon growing from catalysts with no lattice oxygen transfer, of which the former tends to less likely deactivate the catalysts. However, this needs further investigation.

Achieving separable carbons with negligible catalyst content is important to push simultaneous production of hydrogen and solid carbon for practical applications. In this study, we demonstrated fluidisation with higher U/U$_{mf}$ (*e.g.*, 6.1 ± 0.2 at 800°C and 7.2 ± 0.4 at 900°C) allowed the carbon-rich solid fines to be separated from the carbon-lean main particles. According to Davidson and Harrison's formula ($V_b = 1.138G^{6/5}/g^{3/5}$, where V_b is the bubble volume on detachment, G is the volumetric flow rate) [38], higher gas velocities would produce bubbles with large diameter on the detachment from the distributor. In our case, this would generate initial bubbles with a diameter of 12.5 mm at 700 °C to 13.5 mm at 900 °C, close to the FBR internal diameter of 15 mm. At higher temperatures like 900 °C and higher U/U$_{mf}$, a higher fraction of gas flows through the bubbles, creating more bubbles and more vigorous fluidisation. In the small diameter bed used here this results in a more turbulent and chaotic bed. Therefore, during the process of carbon growing on/within the particles, the more turbulent flow structure at higher temperatures will more

easily produce carbon-rich fines by breaking the additional growth from the main particles.

In the retrieved carbon fines from the collection tube, catalyst nanoparticles and amorphous carbon were present, meaning further purification of the structured carbon products would be needed. Using air at 700 °C was effective in removing the amorphous carbon, but a full separation of the structured carbon from the catalysts/support requires further investigation and a better control of carbon formation mechanism. Follow-on studies shall focus on promoting base-growth types of carbon and improving the contact between the catalysts and the main particles. To allow outwards growth and easy break off the structured carbon from the main catalytic particles, in addition to achieve a turbulent flow pattern within the FBR, it is likely that non-porous particles with well distributed catalytic surface will be needed.

5. Conclusions

The simultaneous production of hydrogen and separable carbon-rich solid product was demonstrated in a fluidised bed of $NiO/Ca_2Fe_2O_5/$ CaO particles with CH_4/CO_2 cycles in a temperature range of 700 °C to 900 °C. Carbon growth on the activated $NiO/Ca_2Fe_2O_5/CaO$ particles over the course of reduction within the FBR was tracked and carbon fines were retrieved from the collection tube; both amorphous and structured carbon were observed on particles and solid carbon fines. The retrieved carbon fines had higher carbon content than those on the larger particles within the FBR. The phase transitions observed by XRD and element distributions (TEM-EDX) suggest that the carbon growth over Fe seems to be a result of the combination of multiple mechanisms, including on the Fe_3C sites, and directly on Fe. Higher process temperatures (800 °C and 900 °C), which gave higher U/U_{mf} (*i.e.* 6.1 ± 0.2 at 800°C and 7.2 ± 0.4 at 900°C) and thus more turbulent flow structure, seems to promote separation of solid carbon fines from the fluidised bed of $NiO/Ca_2Fe_2O_5/CaO$ particles. To obtain solid product with more structured carbon (over amorphous carbon), burn-off in air at 700 °C was demonstrated to remove amorphous carbon. It was also noticed that the presence of local lattice oxygen in $Ca_2Fe_2O_5$ increased both the amount of H_2 and solid carbon produced over CH_4 conversion. Future research will follow on maximising the production of separable structured carbon by material design (*e.g.* non-porous support with strong contact with surface catalytic parts) and process optimisation (*e.g.* high U/U_{mf} or high turbulence to allow carbon fines breakdown).

CRediT authorship contribution statement

Karine Alkhatib: Writing – original draft, Investigation, Formal analysis, Data curation. **Made Santihayu Sukma:** Writing – review & editing, Investigation. **Stuart A. Scott:** Writing – review & editing, Supervision, Funding acquisition, Conceptualization. **Yaoyao Zheng:** Writing – review & editing, Writing – original draft, Supervision, Methodology, Formal analysis, Conceptualization.

Declaration of competing interest

The authors declare that they have no known competing financial interests or personal relationships that could have appeared to influence the work reported in this paper.

Data availability

Data will be made available on request.

Acknowledgments

Appendix A. Supplementary material

Supplementary data to this article can be found online at https://doi. org/10.1016/j.fuel.2024.132816.

References

[1] I. - International Energy Agency, Global Hydrogen Review 2023; 2023. www.iea. org (accessed April 8, 2024).

[2] Goodman ED, Latimer AA, Yang AC, Wu L, Tahsini N, Abild-Pedersen F, et al. Low-temperature methane partial oxidation to syngas with modular nanocrystal catalysts. ACS Appl Nano Mater 2018;1:5258–67. https://doi.org/10.1021/ ACSANM.8B01256/ASSET/IMAGES/LARGE/AN-2018-012569_0006.JPEG.

[3] Cleeton JP. Chemical looping combustion with simultaneous power generation and hydrogen production using iron oxides. Cambridge; 2011.

[4] Chiron F-X, Patience GS. Kinetics of mixed copper–iron based oxygen carriers for hydrogen production by chemical looping water splitting. Int J Hydrogen Energy 2012;37:10526–38. https://doi.org/10.1016/j.ijhydene.2012.04.052.

[5] Liu W, Ismail M, Dunstan MT, Hu W, Zhang Z, Fennell PS, et al. Inhibiting the interaction between FeO and Al₂O₃ during chemical looping production of hydrogen. RSC Adv 2015;5:1759–71. https://doi.org/10.1039/C4RA11891J.

[6] Antzara A, Heracleous E, Bukur DB, Lemonidou AA. Thermodynamic analysis of hydrogen production via chemical looping steam methane reforming coupled with in situ CO₂ capture. Int J Greenhouse Gas Control 2015;32:115–28. https://doi. org/10.1016/j.ijggc.2014.11.010.

[7] Sun Z, Chen S, Hu J, Chen A, Rony AH, Russell CK, et al. Ca₂Fe₂O₅: A promising oxygen carrier for CO/CH₄ conversion and almost-pure H₂ production with inherent CO₂ capture over a two-step chemical looping hydrogen generation process. Appl Energy 211 2018:431–42. https://doi.org/10.1016/j. apenergy.2017.11.005.

[8] Luo M, Yi Y, Wang S, Wang Z, Du M, Pan J, et al. Review of hydrogen production using chemical-looping technology. Renew Sustain Energy Rev 2018;81:3186–214. https://doi.org/10.1016/J.RSER.2017.07.007.

[9] B. Niels, B.-S. Adam, Is carbon capture too expensive? – Analysis - IEA, International Energy Agency (IEA) (2021). https://www.iea.org/commentaries/is-carbon-capture-too-expensive (accessed May 15, 2024).

[10] Kim J, Oh C, Oh H, Lee Y, Seo H, Kim YK. Catalytic methane pyrolysis for simultaneous production of hydrogen and graphitic carbon using a ceramic sparger in a molten NiSn alloy. Carbon N Y 2023;207:1–12. https://doi.org/10.1016/J. CARBON.2023.02.053.

[11] Vanderbilt University, Cheap, small carbon nanotubes – ScienceDaily, (2018). https://www.sciencedaily.com/releases/2018/05/180523160148.htm (accessed April 12, 2024).

[12] McConnachie M, Konarova M, Smart S. Literature review of the catalytic pyrolysis of methane for hydrogen and carbon production. Int J Hydrogen Energy 2023;48: 25660–82. https://doi.org/10.1016/J.IJHYDENE.2023.03.123.

[13] Abánades A, Ruiz E, Ferruelo EM, Hernández F, Cabanillas A, Martínez-Val JM, et al. Experimental analysis of direct thermal methane cracking. Int J Hydrogen Energy 2011;36:12877–86. https://doi.org/10.1016/J.IJHYDENE.2011.07.081.

[14] Komatsu N, Wang F. A Comprehensive Review on Separation Methods and Techniques for Single-Walled Carbon Nanotubes. Materials 2010;3:3818. https:// doi.org/10.3390/MA3073818.

[15] Upham DC, Agarwal V, Khechfe A, Snodgrass ZR, Gordon MJ, Metiu H, et al. Catalytic molten metals for the direct conversion of methane to hydrogen and separable carbon. Science 1979;358(2017):917–21. https://doi.org/10.1126/ SCIENCE.AAO5023/SUPPL_FILE/AAO5023S2.MP4.

[16] Geißler T, Plevan M, Abánades A, Heinzel A, Mehravaran K, Rathnam RK, et al. Experimental investigation and thermo-chemical modeling of methane pyrolysis in a liquid metal bubble column reactor with a packed bed. Int J Hydrogen Energy 2015;40:14134–46. https://doi.org/10.1016/J.IJHYDENE.2015.08.102.

[17] Parkinson B, Patzschke CF, Nikolis D, Raman S, Dankworth DC, Hellgardt K. Methane pyrolysis in monovalent alkali halide salts: Kinetics and pyrolytic carbon properties. Int J Hydrogen Energy 2021;46:6225–38. https://doi.org/10.1016/J. IJHYDENE.2020.11.150.

[18] Zheng Y, Sukma MS, Scott SA. The exploration of NiO/Ca₂Fe₂O₅/CaO in chemical looping methane conversion for syngas and H₂ production. Chem Eng J 2023;465: 142779. https://doi.org/10.1016/j.cej.2023.142779.

[19] Kumar M, Kumar M. Carbon Nanotube Synthesis and Growth Mechanism, Carbon Nanotubes - Synthesis, Characterization. Applications 2011. https://doi.org/ 10.5772/19331.

[20] Gohier A, Ewels CP, Minea TM, Djouadi MA. Carbon nanotube growth mechanism switches from tip- to base-growth with decreasing catalyst particle size. Carbon N Y 2008;46:1331–8. https://doi.org/10.1016/J.CARBON.2008.05.016.

[21] Gibson IA, Slim CJ, Zheng Y, Scott SA, Davidson JF, Hayhurst AN. An examination of Wen and Yu's formula for predicting the onset of fluidisation. Chem Eng Res Des 2018;135:103–11. https://doi.org/10.1016/j.cherd.2018.05.009.

[22] D. Zagorac, H. Muller, S. Ruehl, S. Zagorac, J. & Rehme, ICSD, J Appl Crystallogr 52 (2019) 918–925. Doi: 10.1107/S160057671900997X.

[23] Sukma MS, Zheng Y, Hodgson P, Scott SA. Understanding the Behavior of Dicalcium Ferrite (Ca₂Fe₂O₅) in Chemical Looping Syngas Production from CH₄. Energy Fuel 2022;36:9410–22. https://doi.org/10.1021/acs.energyfuels.2c01065.

[24] Kharissova OV, Kharisov BI. Variations of interlayer spacing in carbon nanotubes. RSC Adv 2014;4:30807–15. https://doi.org/10.1039/C4RA04201H.

[25] Fukuhara C, Matsui Y, Tanebayashi M, Watanabe R. A novel catalytic reaction system capturing solid carbon from greenhouse gas, combined with dry reforming of methane. Chemical Engineering Journal Advances 2021;5:100057. https://doi.org/10.1016/J.CEJA.2020.100057.

[26] Wirth CT, Bayer BC, Gamalski AD, Esconjauregui S, Weatherup RS, Ducati C, et al. The phase of iron catalyst nanoparticles during carbon nanotube growth. Chem Mater 2012;24:4633–40. https://doi.org/10.1021/CM301402G/SUPPL_FILE/CM301402G_SI_003.AVI.

[27] Sengupta J, Jacob C. The effect of Fe and Ni catalysts on the growth of multiwalled carbon nanotubes using chemical vapor deposition. J Nanopart Res 2010;12:457–65. https://doi.org/10.1007/S11051-009-9667-1/FIGURES/6.

[28] Wang W, Wang H, Yang Y, Jiang S. Ni–SiO$_2$ and Ni–Fe–SiO$_2$ catalysts for methane decomposition to prepare hydrogen and carbon filaments. Int J Hydrogen Energy 2012;37:9058–66. https://doi.org/10.1016/J.IJHYDENE.2012.03.003.

[29] E. Välimäki, L. Yli-Varo, H. Romar, U. Lassi, Carbons Formed in Methane Thermal and Thermocatalytic Decomposition Processes: Properties and Applications, C 2021, Vol. 7, Page 50 7 (2021) 50. Doi: 10.3390/C7030050.

[30] A. Gamal, K. Eid, M.H. El-Naas, D. Kumar, A. Kumar, Catalytic Methane Decomposition to Carbon Nanostructures and COx-Free Hydrogen: A Mini-Review, Nanomaterials 2021, Vol. 11, Page 1226 11 (2021) 1226. Doi: 10.3390/NANO11051226.

[31] Childres I, Jauregui LA, Park W, Caoa H, Chena YP. Raman spectroscopy of graphene and related materials, in. New Developments in Photon and Materials Research 2013:403–18. https://doi.org/10.1016/b978-0-323-90800-9.00252-3.

[32] Ferrari A, Robertson J. Interpretation of Raman spectra of disordered and amorphous carbon. Phys Rev B 2000;61:14095. https://doi.org/10.1103/PhysRevB.61.14095.

[33] Mera G, Navrotsky A, Sen S, Kleebe HJ, Riedel R. Polymer-derived SiCN and SiOC ceramics – structure and energetics at the nanoscale. J Mater Chem A Mater 2013;1:3826–36. https://doi.org/10.1039/C2TA00727D.

[34] Li Z, Deng L, Kinloch IA, Young RJ. Raman spectroscopy of carbon materials and their composites: Graphene, nanotubes and fibres. Prog Mater Sci 2023;135:101089. https://doi.org/10.1016/J.PMATSCI.2023.101089.

[35] Zhou L, Enakonda LR, Harb M, Saih Y, Aguilar-Tapia A, Ould-Chikh S, et al. Fe catalysts for methane decomposition to produce hydrogen and carbon nano materials. Appl Catal B 2017;208:44–59. https://doi.org/10.1016/J.APCATB.2017.02.052.

[36] Jaworski Z, Zakrzewska B, Pianko-Oprych P. On thermodynamic equilibrium of carbon deposition from gaseous C-H-O mixtures: Updating for nanotubes. Rev Chem Eng 2017;33:217–35. https://doi.org/10.1515/REVCE-2016-0022/ASSET/GRAPHIC/J_REVCE-2016-0022_FIG_002.JPG.

[37] Zheng Y, Marek EJ, Scott SA. H2 production from a plasma-assisted chemical looping system from the partial oxidation of CH4 at mild temperatures. Chem Eng J 2020;379:122197. https://doi.org/10.1016/j.cej.2019.122197.

[38] Davidson JF, Harrison D. Fluidised particles. Cambridge University Press; 1963.